The Journal of Chemical Physics

Fluid–fluid phase transitions in a chiral molecular model

Cite as: J. Chem. Phys. **157**, 084501 (2022); https://doi.org/10.1063/5.0105851
Submitted: 25 June 2022 • Accepted: 01 August 2022 • Accepted Manuscript Online: 05 August 2022 • Published Online: 25 August 2022

Yiming Wang, Frank H. Stillinger and Pablo G. Debenedetti

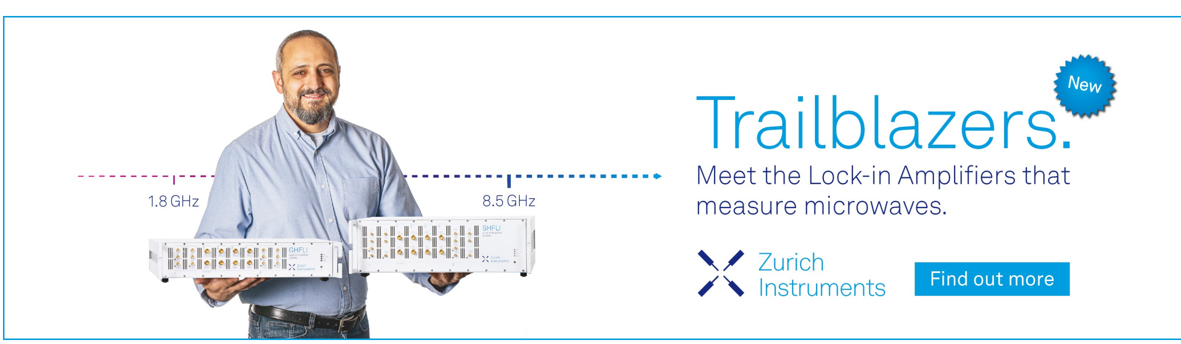

The Journal of Chemical Physics | ARTICLE | scitation.org/journal/jcp

Fluid–fluid phase transitions in a chiral molecular model

Cite as: J. Chem. Phys. 157, 084501 (2022); doi: 10.1063/5.0105851
Submitted: 25 June 2022 • Accepted: 1 August 2022 •
Published Online: 25 August 2022

View Online Export Citation CrossMark

Yiming Wang,[1] Frank H. Stillinger,[2] and Pablo G. Debenedetti[1,a)]

AFFILIATIONS

[1] Department of Chemical and Biological Engineering, Princeton University, Princeton, New Jersey 08544, USA
[2] Department of Chemistry, Princeton University, Princeton, New Jersey 08544, USA

[a)] Author to whom correspondence should be addressed: pdebene@princeton.edu

ABSTRACT

Molecular chirality is a fundamental phenomenon, underlying both life as we know it and industrial pharmaceutical syntheses. Understanding the symmetry breaking phase transitions exhibited by many chiral molecular substances provides basic insights for topics ranging from the origin of life to the rational design of drug manufacturing processes. In this work, we have performed molecular dynamics simulations to investigate the fluid–fluid phase transitions of a flexible three-dimensional four-site chiral molecular model developed by Latinwo *et al.* [J. Chem. Phys. **145**, 154503 (2016)] and Petsev *et al.* [J. Chem. Phys. **155**, 084105 (2021)]. By introducing a bias favoring local homochiral vs heterochiral interactions, the system exhibits a phase transition from a single achiral phase to a single chiral phase that undergoes infrequent interconversion between the two thermodynamically identical chiral states: the L-rich and D-rich phases. According to the phase rule, this reactive binary system has two independent degrees of freedom and exhibits a density-dependent critical locus. Below the liquid–liquid critical locus, there exists a first-order vapor–liquid coexistence region with a single independent degree of freedom. Our results provide basic thermodynamic and kinetic insights for understanding many-body chiral symmetry breaking phenomena.

I. INTRODUCTION

A variety of chemicals are chiral, ranging from inorganic molecules such as hydrogen peroxide, organic ions such as the hexols, to the building blocks of life, including amino acids, nucleotides, and carbohydrates.[1,2] Intriguingly, although the L- and D-enantiomers have the same scalar physicochemical properties, a number of naturally occurring chiral molecules exist in enantiopure form in living systems. For example, in living organisms, all amino acids (except glycine) are L-amino acids while all carbohydrates exist in their D-enantiomeric form.[3] A plausible hypothesis for the emergence of biological homochirality involves the amplification of an initial random small excess of one enantiomer over the other during complex biochemical reaction networks in the racemic prebiotic world.[4–6] However, the exact mechanism for such chiral symmetry breaking phenomena in nature remains a subject of ongoing iniquiry.[3,7,8]

On the laboratory scale, experimental studies have demonstrated that chiral symmetry breaking phenomena can be achieved for a variety of organic and inorganic compounds.[9–11] For organic compounds such as amino acids[12] and inorganic compounds such as sodium chlorate[13] that form chiral crystals, a stochastic chiral autocatalytic amplification is achieved by continuous stirring and mechanical attrition in solution due to the Ostwald ripening effect.[14,15] However, such attrition-induced solid-phase enantioenrichment is a nonequilibrium scenario. Without attrition or stirring, at equilibrium, a conglomerate crystal system is formed out of solution, containing equal amounts of left- and right-handed chiral crystals (physical mixture) if conglomerate (enantiopure) crystals are energetically stable relative to their racemic counterparts (e.g., LDLD).[16] Adding a chiral solvent can also induce mirror symmetry breaking during chiral nanocrystal formation, and the phenomenon has been found to occur through a first-order transition.[16] While most of the reported chiral symmetry breaking phenomena involve crystallization processes, recent experiments[17] suggest that chiral symmetry breaking can also occur during liquid–liquid phase separation of an initially isotropic solution of achiral organic compounds.

A number of theoretical and computational models have been developed to address the thermodynamic and kinetic questions underlying chiral symmetry breaking, chiral phase separation, and crystal polymorphism.[18–23] Motivated by the experimental observation of chiral amplification via liquid–liquid phase transition in an initially anisotropic liquid,[17] Stillinger[24] applied the mean field approximation to a three-dimensional lattice model to investigate its vapor–liquid phase transition and chirality-induced liquid–liquid phase transition, as well as their critical point confluence phenomenon. Previously, Latinwo *et al.*[25] developed a three-dimensional four-site flexible molecular chiral model that differentiates homochiral and heterochiral local interactions via tuning a chiral renormalization parameter to drive liquid–liquid phase separation. Recently, Petsev *et al.*[26] reformulated Latinwo's four-site molecular model by correcting the derivation of the eight-body intermolecular force between tetramer pairs.

A thermodynamic prerequisite to understanding fundamental aspects of chiral symmetry breaking phenomena and chirality-driven phase transitions is to construct a phase diagram that characterizes the state of a system as a function of thermodynamic variables such as pressure, density, and temperature. Although recent work has started to address the liquid–liquid phase behavior of the chiral tetramer model,[27] a systematic study has not been undertaken. In this work, we perform molecular dynamics simulations of the chiral tetramer model developed by Latinwo *et al.*[25] and Petsev *et al.*[26] to investigate the kinetics and thermodynamics underlying its chirality-driven phase transitions and fluid-phase chiral symmetry breaking phenomena. In Sec. II, we provide details of the molecular model and the simulation protocols. In Sec. III, we investigate the temperature, density, and system size dependence of the characteristic time and activation barrier of the chiral phase interconversion events. We also present the system's vapor–liquid and liquid–liquid phase diagram. In Sec. IV, we provide concluding remarks.

II. MODEL AND METHODS

In this work, NVT ensemble molecular dynamics (MD) simulations are performed with the LAMMPS package[26] using a flexible three-dimensional four-site (tetramer) chiral molecular model developed by Latinwo *et al.*[25] and Petsev *et al.*[26] The mass of monomer site (m), bond stretch constant (k_s), and dihedral constant (k_d) are chosen to represent hydrogen peroxide and are summarized in Table S1 (see the supplementary material); these are consistent with the bond vibrational frequencies measured for hydrogen peroxide.[28–30] Of course, the actual values of the parameters are only relevant if the results need to be mapped to actual thermodynamic conditions (i.e., temperature, rather than scaled temperature). The four monomer sites along each tetramer bond backbone are represented as Lennard-Jones (LJ) pair interaction centers with energy and length parameters ε_0 and σ_0. A time step of 0.001 t^* was used for the velocity Verlet integrator [$t^* = \sigma_0(m/\varepsilon_0)^{1/2}$, see Table S1 (supplementary material)]. The system number density ($\rho = N/V$) is defined as the total number of tetramer molecules divided by the system volume in reduced units $\left[\rho^* = \rho\sigma_0^3\right]$. The temperature ($T^* = k_B T/\varepsilon_0$) was maintained using a Nosé–Hoover thermostat.[31,32] Periodic boundary conditions were applied in all three directions of a cubic simulation box. In addition, we apply the scalar chirality measure ζ to identify the L- and D-enantiomers (see Fig. S1),

$$\zeta(\mathbf{r}_1,\mathbf{r}_2,\mathbf{r}_3,\mathbf{r}_4) = \frac{\mathbf{r}_{12}\cdot(\mathbf{r}_{23}\times\mathbf{r}_{34})}{|\mathbf{r}_{12}||\mathbf{r}_{23}||\mathbf{r}_{34}|}, \tag{1}$$

where $\mathbf{r}_1, \mathbf{r}_2, \mathbf{r}_3, \mathbf{r}_4$ are the vectors from the laboratory-frame coordinate origin to each of the four sites of the chiral tetramer molecule, as defined by Latinwo *et al.*[25] One has $-1 \le \zeta \le +1$, and $\zeta_L < 0$ and $\zeta_D > 0$. The overall system composition is conveniently characterized by the enantiomeric excess (ee),

$$ee = x_L - x_D = \frac{n_L - n_D}{n_L + n_D}, \tag{2}$$

where n_L and n_D are, respectively, the total number of L- and D-enantiomers determined by the sign of the scalar chirality measure ζ of each tetramer molecule in the system.

One of the key features of this chiral model is the fact that the site–site interaction potential between monomers i and j, belonging to distinct tetramers A and B, is a multibody potential renormalized in a manner distinct from the conventional Lennard-Jones 12-6 potential, via

$$\begin{aligned} U_{ij}\left(\zeta^A,\zeta^B\right) &= \left(1+\lambda\zeta^A\zeta^B\right)\varepsilon_0\cdot U_{LJ}(r_{ij}) \\ &= \left(1+\lambda\zeta^A\zeta^B\right)\varepsilon_0\cdot 4\left[\left(\frac{\sigma_0}{r_{ij}}\right)^{12} - \left(\frac{\sigma_0}{r_{ij}}\right)^{6}\right], \end{aligned} \tag{3}$$

where ε_0 and σ_0 are the energetic and geometric parameters of the Lennard-Jones (LJ) potential in Table I. Here, ζ^A and ζ^B are the scalar chirality values for tetramer molecules A and B. The chiral renormalization parameter λ acts to favor local homochiral ($\lambda > 0$) or heterochiral ($\lambda < 0$) interactions. For computational purposes, the site–site LJ potential is shifted by a constant value, goes to zero at a cutoff distance r_c, and remains zero for $r > r_c$. In order to keep the effect of the resulting slope discontinuity numerically negligible, the cutoff distance in this work was chosen to be $r_c = 4\sigma_0$. Due to the fact that the scalar chirality ζ measure is a function of the position of all four monomers on a tetramer, the intermolecular force $\mathbf{F}_k$ experienced by a given monomer k on tetramer A when interacting with tetramer B must be written as the negative gradient of the entire A plus B molecular pair potential with respect to the monomer position vector $\mathbf{r}_k$. Here, k could be any one of the four sites on tetramer A,

$$\begin{aligned} \mathbf{F}_k^A &= \sum_{i=1}^{4}\sum_{j=1}^{4}\left[-\frac{\partial U_{ij}\left(\zeta^A,\zeta^B\right)}{\partial \mathbf{r}_k^A}\right] \\ &= \sum_{i=1}^{4}\sum_{j=1}^{4}\left[-\left(1+\lambda\zeta^A\zeta^B\right)\varepsilon_0\frac{\partial U_{LJ}(r_{ij})}{\partial \mathbf{r}_k^A} - \lambda\zeta^B\varepsilon_0 U_{LJ}(r_{ij})\frac{\partial \zeta^A}{\partial \mathbf{r}_k^A}\right]. \end{aligned} \tag{4}$$

The chain rule is then applied to split the total force into two parts. The first term originates from the conventional LJ force and the second term is a multibody (eight-body) force term, called lambda force, that acts between all eight monomers of a given tetramer pair. The detailed derivation of the multibody intermolecular forces is described in the work of Petsev *et al.*[26]

III. RESULTS AND DISCUSSION

We first investigate the chirality-driven liquid phase behavior of this model system over a range of temperatures, at a reduced tetramer number density $\rho^* = 0.11$. As shown in Fig. 1, at $T^* > 4.6$, the system is an achiral liquid mixture of L- and D-enantiomers (ee = 0). At this density, the liquid–liquid critical temperature is close to $T^* = 4.6$, as can be seen by the pronounced enhancement of ee fluctuations. Upon phase separation, the system exhibits stochastic symmetry breaking alternatively into the L-rich state with large positive ee or the D-rich state with large negative ee, so that, at sufficiently long times, the observed distribution of the order parameter ee switches from unimodal to bimodal. The driving force for this phase transition is the choice of a positive chiral renormalization parameter $\lambda = 0.5$, favoring local homochiral interactions and disfavoring heterochiral interactions.

The key feature of this chirality-driven phase transition is that the whole system exhibits infrequent interconversion between the two thermodynamically identical chiral states (L-rich and D-rich), without a direct (stable) coexistence of the two states, as shown in Fig. 1(b). This phase transition system is different from the liquid–liquid phase transitions of conventional binary mixture such as oil and water.[33] It is also different from single-component molecular systems reported in the literature, such as supercooled water,[34–36] supercooled silicon,[37,38] and sulfur,[39] wherein there exists a direct coexistence of two thermodynamically distinct phases, e.g., the high and the low density liquid phases.

Because the number of L or D molecules is a non-conserved quantity, the system can avoid the energetic penalty associated with the formation of an interface ($\lambda > 0$ case) by forming, at any given time, either the L-rich or the D-rich phase. In this sense, the transition implied by the bimodal ee distributions shown in Fig. 1(a) is degenerate, there being no true coexistence between immiscible phases, but rather random fluctuations (in a finite system) between the stable L-rich and its symmetric D-rich counterpart.

To investigate the temperature, density, and system size dependence of the chiral phase interconversion kinetics, we calculated the time autocorrelation function for the system's ee for $T^* = 3$–5, $\rho^* = 0.07$–0.13, and N = 500–4000 using

$$C_{ee}(\Delta t) = \frac{\langle ee(t+\Delta t)\cdot ee(t)\rangle}{\langle ee(t)\cdot ee(t)\rangle}. \tag{5}$$

The $C_{ee}(\Delta t)$ profile is then fitted to an exponential function $C_{ee}(\Delta t) = e^{-\Delta t/\tau_{in}}$ (see Fig. S2). The physical meaning of τ_{in} is the characteristic time during which the system stays in one chiral phase before it randomly converts to the other chiral phase. τ_{in} provides an estimate of the characteristic chiral phase interconversion time. As shown in Fig. 2(a), τ_{in} shows a simple Arrhenius temperature dependence,

$$\tau_{in} = \tau_0 \exp\left(\frac{\Delta G_{in}}{k_{\mathbf{B}}T}\right), \tag{6}$$

where τ_0 is the reference time, k_B is the Boltzmann constant, and ΔG_{in} is the free energy barrier. Equation (6) has been applied to calculate the energy barrier and transition path time for the folding of native proteins.[40] From Fig. 2(b), the activation barrier ΔG_{in} increases with increasing density, reflecting the fact that the average attraction strength felt by each tetramer with respect to its neighbors increases with increasing density. This explains why the model system has very infrequent conversion between the L-rich and D-rich states at sufficiently subcritical temperatures [Fig. 1(a)]. In

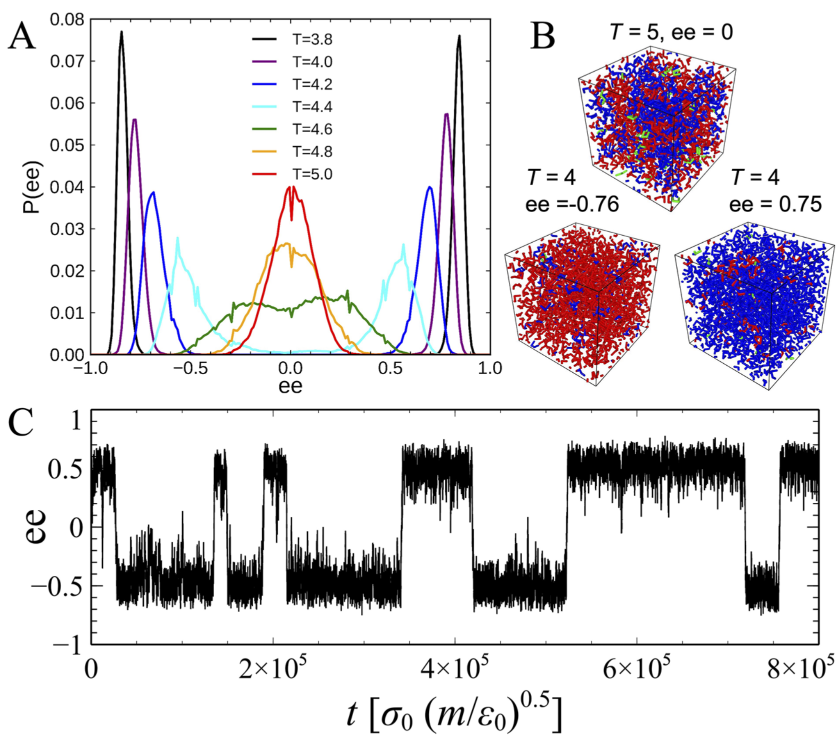

FIG. 1. (a) Distribution of overall enantiomeric excess (ee) during the chirality-driven liquid–liquid phase separation at chiral renormalization parameter $\lambda = 0.5$, density $\rho^* = 0.11$, and $T^* = 3.8$–5.0. (b) Simulation snapshots taken for the achiral state at $T^* = 5$ and two symmetric chiral states at $T^* = 4$. Color scheme: L enantiomer with $\zeta < -0.3$, D enantiomer with $\zeta > 0.3$, and molecules in "transition state" with $|\zeta| \leq 0.3$ are colored blue, red, and green, respectively. (c) Time-dependent behavior of the enantiomeric excess at $\rho^* = 0.11$ and $T^* = 4.45$.

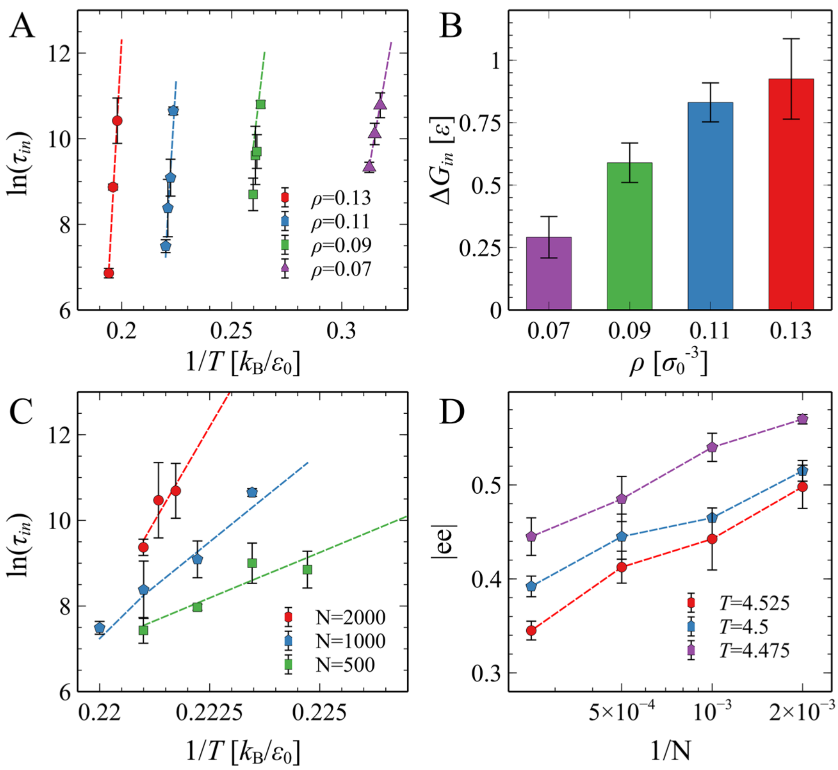

FIG. 2. Characteristic time τ_{in} (a) and activation barrier ΔG_{in} (b) of chiral phase interconversion for $\rho^* = 0.07$–0.13, $\lambda = 0.5$ and N = 1000. System size dependence of τ_{in} (c) and equilibrium enantiomeric excess, ee (d) at $\rho^* = 0.11$, $T^* = 4.475$–4.525, and N = 500–4000.

addition, from Fig. 2(c), it can be seen that τ_{in} increases with increasing system size. This trend is the opposite to expectations based on classical nucleation theory. The main reason is that in transitioning from the L-rich to the D-rich phase and vice versa, the system necessarily needs to go through an ee = 0 transition state, where energetically unfavorable L-D interactions are maximized. The size of the energetically unfavorable interface between the L-rich and D-rich clusters of this transition state *increases* with increasing system size, in principle as $N^{2/3}$. Finally, in Fig. 2(d), we show that the |ee| decreases with increasing system size. This is because the critical temperature decreases with increasing system size, as expected for phase transitions in finite systems.

Next, we investigate the thermodynamic behavior of this chiral molecular model over a wide range of fluid phase conditions. We first fit the ee-T^* data to the Flory–Huggins nonideal mixing theory[41] to estimate the critical temperature for each isochore in Fig. 3(a),

$$ee = \tanh\left(\frac{\chi \cdot ee}{2}\right), \tag{7}$$

where χ is the Flory–Huggins parameter and its temperature dependence is described by $\chi = a + \frac{b}{T^*}$.[41] Here, a and b are fitting parameters.

As shown in Fig. 3(a), this model system has a critical temperature locus that increases with increasing density. The phase behavior shown in Fig. 3(a) is consistent with a single-phase binary mixture with one chemical reaction. According to the Gibbs phase rule, such a system has two degrees of freedom. As shown in Fig. 3(a), both temperature and density must be specified to describe the system's behavior. As explained above [see Fig. 1(c)], the system exhibits degenerate behavior, such that, at any given subcritical temperature, the pair of symmetric L- and D-rich phases along the "coexistence" curve do not physically coexist. At any given time, there is a single (L- or D-rich) phase. A fuller discussion of the Gibbs phase rule and its application to the present system can be found in the Appendix.

Next, we have computed the first-order vapor–liquid phase boundary of the model system. The liquid–vapor coexistence densities at each temperature are determined simultaneously by calculating the distribution of local densities of the two-phase system and, then, locating the two peak densities from the bimodal local density distributions, as shown in Fig. S3. The center of each spherical sampling volume is randomly placed, and the radius within which the density is determined is chosen to be $5\sigma_0$. The so-obtained temperature-dependent vapor–liquid coexistence density data are then fitted to a power law scaling equation using the three-dimensional Ising model critical exponent[42] to locate the vapor–liquid critical point, which gives $T_c = 2.7$ and $\rho_c = 0.067$ for the $\lambda = 0.5$ case.

$$\rho_L - \rho_V = \Delta\rho_0\left(1 - \frac{T}{T_c}\right)^{\beta}, \tag{8}$$

$$\frac{\rho_L + \rho_V}{2} = \rho_c + D(T - T_c), \tag{9}$$

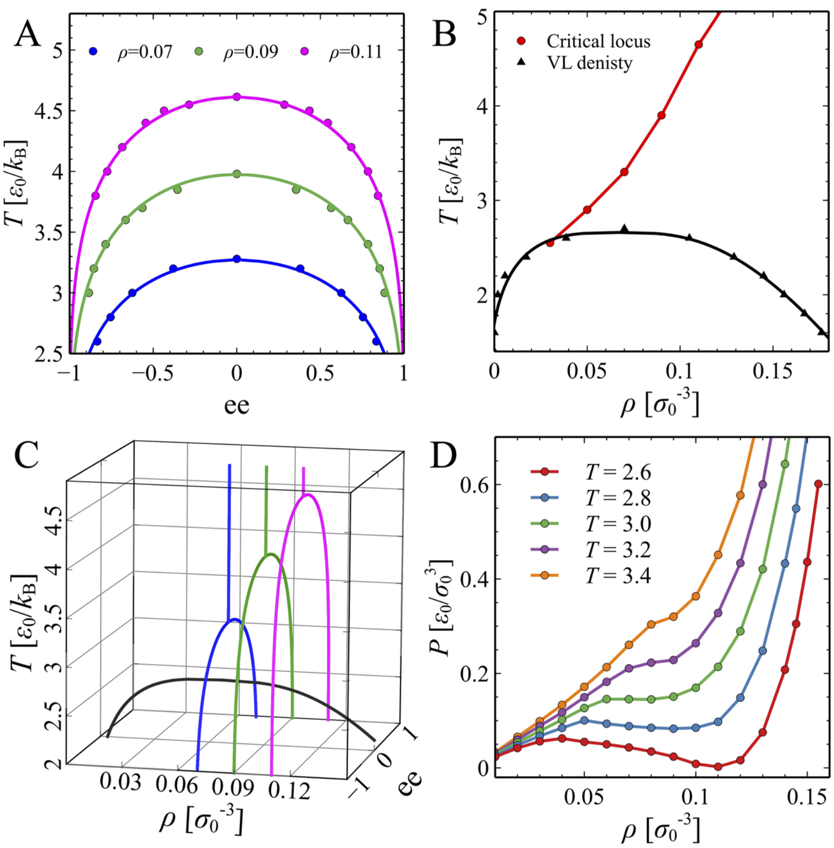

FIG. 3. Phase diagram of the chiral molecular model for $\lambda = 0.5$. (a) Equilibrium ee as a function of temperature for $\rho^* = 0.07$, 0.09, and 0.11, respectively. The filled circles are equilibrium ee values measured at different temperatures from NVT simulations and the lines are obtained by fitting the ee vs T^* data to the thermodynamic non-ideal mixing theory using Eq. (7). (b) The liquid–liquid critical locus (red) and the vapor–liquid coexistence boundary (black). (c) Temperature–density–composition (ee) phase diagram. The black solid line is a fitted vapor–liquid coexistence locus using Eqs. (8) and (9), from Fig. 3(b). The blue, green, and purple lines are fitted liquid–liquid phase boundaries in the ee-T^* plane from Fig. 3(a). (d). Pressure–density equation of state for isotherms $T^* = 2.6$–3.4.

where ρ_V and ρ_L are coexistence densities for vapor and liquid phases. $\beta \approx 0.325$ is the critical exponent of three-dimensional Ising model.[43] Equation (9) is the so-called law of rectilinear diameters. It breaks down very close to the critical point, although it is good enough for our purposes. $\Delta\rho_0$ and A are system-specific fitting parameters. As shown in Fig. 3(b), above the vapor–liquid critical point, the system behaves as a homogeneous fluid and has two independent degrees of freedom. Upon vapor–liquid phase separation, the system has an achiral vapor phase in coexistence with a single chiral liquid phase that experiences infrequent interconversion between the L-rich and D-rich states, and the system has only one independent degree of freedom.

We also investigate the influence of the chirality-induced phase transition on the pressure–density equation of state. As shown in Fig. 3(d), the pressure–density equation of state at $T^* = 2.6$ involves a van der Waals loop, which is similar to the vapor–liquid coexistence region of a finite-size Lennard-Jones fluid system.[44] The main difference between the LJ fluid system and the present chiral tetramer model is that along each isotherm for $T^* \geq 2.8$, there exists a density-dependent kink in the pressure–density profile. The possible explanation for observing such density-dependent kinks is that upon increasing density along each isotherm above $T^* = 2.8$, the system crosses the liquid–liquid critical locus and exhibits chiral symmetry breaking. The enhanced homochiral interaction and forces between neighbor tetramers pairs in a chiral (D-rich or L-rich) environment as opposed to the racemic environment leads to a sudden change in the system's isothermal pressure–density relationship.

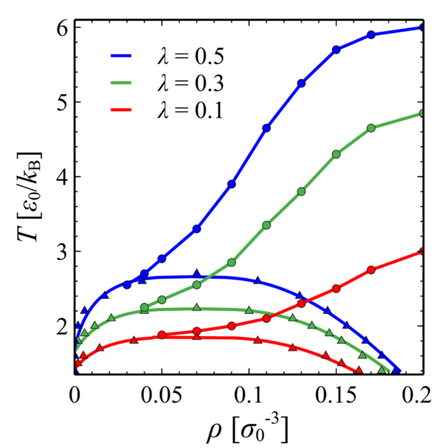

FIG. 4. Temperature–density phase diagram for $\lambda = 0.1$, 0.3, and 0.5. The domes correspond to vapor–liquid equilibrium, and the lines are critical loci for the liquid–liquid transition.

Finally, we evaluate the effect of the positive chiral renormalization parameter λ on the phase transition behavior of the model system, since λ determines the strength of intermolecular interaction and, thus, controls the driving force for phase separation. As shown in Fig. 4, the critical temperature at a given density increases with increasing λ as a result of favoring homochiral and disfavoring heterochiral interactions. Notably, the relative locations of the vapor–liquid critical point and the liquid–liquid critical locus are very sensitive to the choice of λ. As λ decreases, the intersection point between the vapor–liquid coexistence line and liquid–liquid critical locus approaches the vapor–liquid critical point.

IV. CONCLUSION

We have investigated phase transitions in a chiral tetramer model with a finite and tunable interconversion barrier between the two enantiomers. A tunable chiral renormalization parameter controls the energetic preference (penalty) for homochiral (heterochiral) nearest-neighbor interactions. At sufficiently low temperatures, this energetic bias favors liquid–liquid phase separation. Because the enantiomers can interconvert, the system avoids forming an energetically costly interface, and one observes only one equilibrium phase at any given time. The system randomly chooses between the two symmetric "coexisting" phases, and in a finite system such as the one we consider here, it experiences random fluctuations between the symmetric (L- and D-rich) phases. We call this virtual coexistence degenerate behavior. As anticipated theoretically,[24] the system also exhibits first-order coexistence between an achiral vapor and a chiral liquid phase, the latter fluctuating between its two equivalent mirror-image realizations. The Gibbs phase rule provides a convenient framework for interpreting counterintuitive behavior, such as degenerate two-phase coexistence with only one phase present at any given time. Our results provide basic kinetic and thermodynamic insights that may prove helpful in developing a deeper understanding many-body chiral symmetry breaking phenomena.

Future avenues of inquiry include the investigation of low-temperature crystal phases for this model and, in particular, the identification of regions of stability of racemic and conglomerate phases. Also of interest is the investigation of the microscopic mechanisms underlying phase flipping, aspects of which are counter to familiar behavior as described by classical nucleation theory. Both lines of inquiry are presently under investigation.

SUPPLEMENTARY MATERIAL

See the supplementary material for additional information on molecular model parameters and representations; calculation of autocorrelation function for the time-dependent system ee at $\rho^* = 0.11$; probability distribution of local density at $\rho^* = 0.07$–0.11 and $T^* = 2.0$–2.8 for $\lambda = 0.5$; comparison of time scales of L/D conformer interconversion and system relaxation at different temperatures for $\lambda = 0.5$; and convergence check of vapor–liquid coexistence simulation for $\lambda = 0.5$.

ACKNOWLEDGMENTS

P.G.D. acknowledges the support of the National Science Foundation (Award No. CHE-1856704). Simulations were performed on computational resources managed and supported by Princeton Research Computing, a consortium of groups including the Princeton Institute for Computational Science and Engineering (PICSciE) and the Office of Information Technology's High Performance Computing Center and Visualization Laboratory at Princeton University. We thank Nikolai Petsev, Betul Uralcan, and Folarin Latinwo for helpful discussions.

AUTHOR DECLARATIONS

Conflict of Interest

The authors have no conflicts to disclose.

Author Contributions

Yiming Wang: Conceptualization (equal); Data curation (equal); Formal analysis (equal); Investigation (equal); Validation (equal); Visualization (equal); Writing – original draft (equal); Writing – review & editing (equal). **Frank H. Stillinger**: Conceptualization (equal); Methodology (equal); Writing – review & editing (equal). **Pablo G. Debenedetti**: Conceptualization (equal); Funding acquisition (equal); Investigation (equal); Project administration (equal); Supervision (equal); Writing – review & editing (equal).

DATA AVAILABILITY

The data that support the findings of this study are available from the corresponding author upon reasonable request.

APPENDIX: PHASE RULE

The thermodynamic behavior of this chiral molecular system can be well explained by the Gibbs phase rule, which states that the number of independent thermodynamic variables (degrees of freedom, L) is equal to the number of components (C) plus two minus the sum of the number of coexisting phases (π) and the number of linearly independent chemical reactions (R). This model is a reactive binary mixture, thus C = 2 and R = 1. For Fig. 5(a), along the binodal line, the system only adopts one chiral phase at any given time ($\pi = 1$, $|ee| > 0$), and there is no direct coexistence between L-rich and D-rich chiral phases, as explained in the main text. The number of degrees of freedom is two ($L = C + 2 - \pi - R = 2 + 2 - 1 - 1 = 2$), e.g., both temperature and density need to be specified to describe the system's behavior along the degenerate "coexistence" locus. The corresponding behavior in the (P, T) plane is shown in Fig. 5(b). For Figs. 5(c) and 5(d), in the supercritical region, the system is in the achiral phase ($\pi = 1$, ee = 0) and also has two independent degrees of freedom ($L = C + 2 - \pi - R = 2 + 2 - 1 - 1 = 2$). This is why this model system has a critical locus instead of a single critical point.

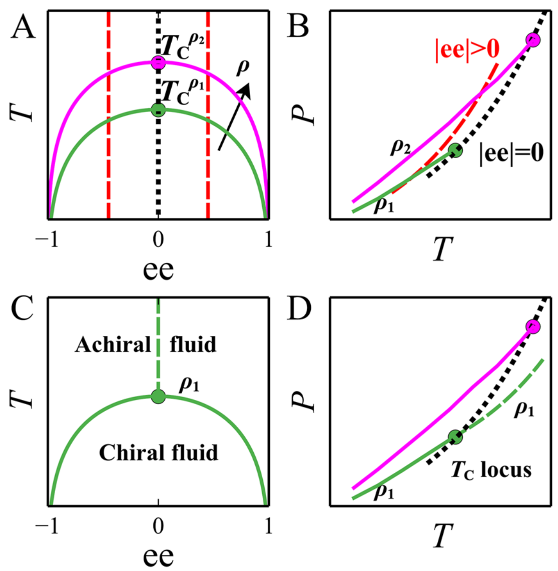

FIG. 5. Schematic phase diagrams for the chiral molecular model in temperature–composition (ee) and pressure–temperature planes based on simulation data. The dashed black line in A, B, and D is the critical locus. Dashed red lines in A and B denote a locus of constant |ee|. The dashed green line in C and D denotes the supercritical homogeneous achiral liquid at density ρ_1.

REFERENCES

[1] R. Ball and J. Brindley, "The life story of hydrogen peroxide II: A periodic pH and thermochemical drive for the RNA world," J. R. Soc., Interface **12**(109), 20150366 (2015).

[2] M. Frenkel-Pinter, M. Samanta, G. Ashkenasy, and L. J. Leman, "Prebiotic peptides: Molecular hubs in the origin of life," Chem. Rev. **120**(11), 4707–4765 (2020).

[3] D. G. Blackmond, "The origin of biological homochirality," Cold Spring Harbor Perspect. Biol. **2**(5), a002147 (2010).

[4] D. G. Blackmond, "Asymmetric autocatalysis and its implications for the origin of homochirality," Proc. Natl. Acad. Sci. U. S. A. **101**(16), 5732–5736 (2004).

[5] N. A. Hawbaker and D. G. Blackmond, "Energy threshold for chiral symmetry breaking in molecular self-replication," Nat. Chem. **11**(10), 957–962 (2019).

[6] M. H. Todd, "Asymmetric autocatalysis: Product recruitment for the increase in the chiral environment (PRICE)," Chem. Soc. Rev. **31**(4), 211–222 (2002).

[7] K. Ruiz-Mirazo, C. Briones, and A. de la Escosura, "Prebiotic systems chemistry: New perspectives for the origins of life," Chem. Rev. **114**(1), 285–366 (2014).

[8] J. Skolnick, H. Zhou, and M. Gao, "On the possible origin of protein homochirality, structure, and biochemical function," Proc. Natl. Acad. Sci. U. S. A. **116**(52), 26571–26579 (2019).

[9] C. Viedma, J. E. Ortiz, T. de Torres, T. Izumi, and D. G. Blackmond, "Evolution of solid phase homochirality for a proteinogenic amino acid," J. Am. Chem. Soc. **130**(46), 15274–15275 (2008).

[10] D. K. Kondepudi, R. J. Kaufman, and N. Singh, "Chiral symmetry-breaking in sodium-chlorate crystallization," Science **250**(4983), 975–976 (1990).

[11] S. M. Morrow, A. J. Bissette, and S. P. Fletcher, "Transmission of chirality through space and across length scales," Nat. Nanotechnol. **12**(5), 410–419 (2017).

[12] J. E. Hein, B. Huynh Cao, C. Viedma, R. M. Kellogg, and D. G. Blackmond, "Pasteur's tweezers revisited: On the mechanism of attrition-enhanced deracemization and resolution of chiral conglomerate solids," J. Am. Chem. Soc. **134**(30), 12629–12636 (2012).

[13] C. Viedma, "Chiral symmetry breaking during crystallization: Complete chiral purity induced by nonlinear autocatalysis and recycling," Phys. Rev. Lett. **94**(6), 065504 (2005).

[14] W. L. Noorduin, H. Meekes, W. J. P. van Enckevort, A. Millemaggi, M. Leeman, B. Kaptein, R. M. Kellogg, and E. Vlieg, "Complete deracemization by attrition-enhanced Ostwald ripening elucidated," Angew. Chem., Int. Ed. **47**(34), 6445–6447 (2008).

[15] W. L. Noorduin, W. J. P. van Enckevort, H. Meekes, B. Kaptein, R. M. Kellogg, J. C. Tully, J. M. McBride, and E. Vlieg, "The driving mechanism behind attrition-enhanced deracemization," Angew. Chem., Int. Ed. **49**(45), 8435–8438 (2010).

[16] U. Hananel, A. Ben-Moshe, H. Diamant, and G. Markovich, "Spontaneous and directed symmetry breaking in the formation of chiral nanocrystals," Proc. Natl. Acad. Sci. U. S. A. **116**(23), 11159–11164 (2019).

[17] C. Dressel, T. Reppe, M. Prehm, M. Brautzsch, and C. Tschierske, "Chiral self-sorting and amplification in isotropic liquids of achiral molecules," Nat. Chem. **6**(11), 971–977 (2014).

[18] J. E. Carpenter and M. Grünwald, "Heterogeneous interactions promote crystallization and spontaneous resolution of chiral molecules," J. Am. Chem. Soc. **142**(24), 10755–10768 (2020).

[19] I. Paci, I. Szleifer, and M. A. Ratner, "Chiral separation: Mechanism modeling in two-dimensional systems," J. Am. Chem. Soc. **129**(12), 3545–3555 (2007).

[20] P. F. Damasceno, A. S. Karas, B. A. Schultz, M. Engel, and S. C. Glotzer, "Controlling chirality of entropic crystals," Phys. Rev. Lett. **115**(15), 158303 (2015).

[21] A. P. Gantapara, W. Qi, and M. Dijkstra, "A novel chiral phase of achiral hard triangles and an entropy-driven demixing of enantiomers," Soft Matter **11**(44), 8684–8691 (2015).

[22] T. G. Lombardo, F. H. Stillinger, and P. G. Debenedetti, "Thermodynamic mechanism for solution phase chiral amplification via a lattice model," Proc. Natl. Acad. Sci. U. S. A. **106**(36), 15131–15135 (2009).

[23] F. Ricci, F. H. Stillinger, and P. G. Debenedetti, "A computational investigation of attrition-enhanced chiral symmetry breaking in conglomerate crystals," J. Chem. Phys. **139**(17), 174503 (2013).

[24] F. H. Stillinger, "Critical point confluence phenomenon," J. Phys. Chem. B **122**(13), 3441–3446 (2018).

[25] F. Latinwo, F. H. Stillinger, and P. G. Debenedetti, "Molecular model for chirality phenomena," J. Chem. Phys. **145**(15), 154503 (2016).

[26] N. D. Petsev, F. H. Stillinger, and P. G. Debenedetti, "Effect of configuration-dependent multi-body forces on interconversion kinetics of a chiral tetramer model," J. Chem. Phys. **155**(8), 084105 (2021).

[27] B. Uralcan, T. J. Longo, M. A. Anisimov, F. H. Stillinger, and P. G. Debenedetti, "Interconversion-controlled liquid–liquid phase separation in a molecular chiral model," J. Chem. Phys. **155**(20), 204502 (2021).

[28] P. A. Giguére and T. K. K. Srinivasan, "A Raman study of H_2O_2 and D_2O_2 vapor," J. Raman Spectrosc. **2**(2), 125–132 (1974).

[29] P. A. Giguère and T. K. K. Srinivasan, "Raman study of matrix isolated H_2O_2 and D_2O_2," Chem. Phys. Lett. **33**(3), 479–482 (1975).

[30] R. H. Hunt, R. A. Leacock, C. W. Peters, and K. T. Hecht, "Internal-rotation in hydrogen peroxide: The far-infrared spectrum and the determination of the hindering potential," J. Chem. Phys. **42**(6), 1931–1946 (1965).

[31] S. Nosé, "A molecular dynamics method for simulations in the canonical ensemble," Mol. Phys. **52**(2), 255–268 (1984).

[32] W. G. Hoover, "Canonical dynamics: Equilibrium phase-space distributions," Phys. Rev. A **31**(3), 1695–1697 (1985).

[33] L. Tang, "Liquid phase separation," Nat. Methods **16**(1), 18 (2019).

[34] J. C. Palmer, F. Martelli, Y. Liu, R. Car, A. Z. Panagiotopoulos, and P. G. Debenedetti, "Metastable liquid–liquid transition in a molecular model of water," Nature **510**(7505), 385–388 (2014).

[35] P. G. Debenedetti, F. Sciortino, and G. H. Zerze, "Second critical point in two realistic models of water," Science **369**(6501), 289–292 (2020).

[36] K. H. Kim, K. Amann-Winkel, N. Giovambattista, A. Späh, F. Perakis, H. Pathak, M. L. Parada, C. Yang, D. Mariedahl, T. Eklund, T. J. Lane, S. You, S. Jeong, M. Weston, J. H. Lee, I. Eom, M. Kim, J. Park, S. H. Chun, P. H. Poole, and A. Nilsson, "Experimental observation of the liquid-liquid transition in bulk supercooled water under pressure," Science **370**(6519), 978–982 (2020).

[37] S. Sastry and C. Austen Angell, "Liquid–liquid phase transition in supercooled silicon," Nat. Mater. **2**(11), 739–743 (2003).
[38] V. V. Vasisht, S. Saw, and S. Sastry, "Liquid–liquid critical point in supercooled silicon," Nat. Phys. **7**(7), 549–553 (2011).
[39] L. Henry, M. Mezouar, G. Garbarino, D. Sifré, G. Weck, and F. Datchi, "Liquid–liquid transition and critical point in sulfur," Nature **584**(7821), 382–386 (2020).
[40] H. S. Chung, K. McHale, J. M. Louis, and W. A. Eaton, "Single-molecule fluorescence experiments determine protein folding transition path times," Science **335**(6071), 981–984 (2012).
[41] M. Rubinstein and R. H. Colby, *Polymer Physics* (Oxford University Press, 2003).
[42] A. Statt, H. Casademunt, C. P. Brangwynne, and A. Z. Panagiotopoulos, "Model for disordered proteins with strongly sequence-dependent liquid phase behavior," J. Chem. Phys. **152**(7), 075101 (2020).
[43] J. S. Rowlinson and B. Widom, *Molecular Theory of Capillarity* (Clarendon Press, Oxford, 1982).
[44] K. Binder, B. J. Block, P. Virnau, and A. Tröster, "Beyond the Van Der Waals loop: What can be learned from simulating Lennard-Jones fluids inside the region of phase coexistence," Am. J. Phys. **80**(12), 1099–1109 (2012).